

This is an Open Access document downloaded from ORCA, Cardiff University's institutional repository: <https://orca.cardiff.ac.uk/id/eprint/112530/>

This is the author's version of a work that was submitted to / accepted for publication.

Citation for final published version:

Jossou, Ericmoore, Eduok, Ubong, Dzade, Nelson Y. , Szpunar, Barbara and Szpunar, Jerzy A. 2018. Oxidation behaviour of U_3Si_2 : an experimental and first principles investigation. *Physical Chemistry Chemical Physics* 20 (7) , pp. 4708-4720.
10.1039/C7CP07154J

Publishers page: <http://dx.doi.org/10.1039/C7CP07154J>

Please note:

Changes made as a result of publishing processes such as copy-editing, formatting and page numbers may not be reflected in this version. For the definitive version of this publication, please refer to the published source. You are advised to consult the publisher's version if you wish to cite this paper.

This version is being made available in accordance with publisher policies. See <http://orca.cf.ac.uk/policies.html> for usage policies. Copyright and moral rights for publications made available in ORCA are retained by the copyright holders.



Oxidation behaviour of U_3Si_2 : an experimental and first principles investigation

Ericmoore Jossou,  ^a Ubong Eduok,  ^a Nelson Y. Dzade,  ^b Barbara Szpunar^c and Jerzy A. Szpunar^a

Uranium-containing metallic systems such as U_3Si_2 are potential Accident Tolerant Fuels (ATFs) for Light Water Reactors (LWRs) and the next generation of nuclear reactors. Their oxidation behaviour, especially in oxygen and water-enriched environments, plays a critical role in determining their applicability in commercial reactors. In this work, we have investigated the oxidation behaviour of U_3Si_2 experimentally and by theoretical computation. The appearance of oxide signatures has been established from X-ray diffraction (XRD) and Raman spectroscopic techniques after oxidation of the solid U_3Si_2 sample in synthetic air (oxygen and nitrogen). We have also studied the changes in the electronic structure as well as the energetics of oxygen interactions on the U_3Si_2 surfaces using first principles calculations in the Density Functional Theory (DFT) formalism. The detailed charge transfer and bond length analyses revealed the preferential formation of mixed oxides of UO_2 and SiO_2 on the $\text{U}_3\text{Si}_2\{001\}$ surface as well as UO_2 alone on the $\text{U}_3\text{Si}_2\{110\}$ and $\{111\}$ surfaces. The formation of the peroxo (O_2^{2-}) state confirmed the dissociation of molecular oxygen before U_3Si_2 oxidation. Core experimental analyses of the oxidized U_3Si_2 samples have revealed the formation of higher oxides from Raman spectroscopy and XRD techniques. This work is introduced to further a better understanding of the oxidation of U–Si metallic fuel compounds.

1. Introduction

Uranium silicides have attracted significant scientific interest in recent times owing to their potential as a replacement for uranium dioxide (UO_2) fuel in commercial light water reactors (LWRs), and by extension can be used in supercritical water reactors (SCWRs). Due to its high thermal conductivity which increases with temperature, high uranium density (11.3 g U cm^{-3}) and irradiation behavior, uranium sesquioxide (U_3Si_2) has become a material of interest for generation IV nuclear reactors.^{1–4} U–Si compounds and metallic fuels in general, however, easily get oxidized when in contact with oxygen and water, making them difficult to characterize.⁵ Furthermore, as a nuclear fuel for commercial reactors, there is a minimum performance requirement in the presence of oxygen, a water enriched environment, radiation and temperature. This has prompted the need to rigorously investigate the thermal properties and oxidation

behavior of U_3Si_2 in water and in an oxygenated environment using both experimental and theoretical techniques.

Earlier investigations of the oxidation behaviour of U_3Si_2 (alongside USi and U_3Si_5) between room temperature and 1000 °C revealed that UO_2 is preferentially formed⁶ and inhibits the formation of a passivating SiO_2 layer that is expected to serve as a protective barrier in the UN– U_3Si_2 composite.⁷ This inference was reached based on thermodynamics argument and we posit further investigation of this behavior from an atomistic perspective with the aim of providing a fundamental understanding of the oxidation of the U_3Si_2 fuel material. Previous theoretical calculations of the surface properties and compositions of actinide-bearing compounds have focused extensively on UN, UO_2 and PuO_2 .^{8–12} According to a recent ATF-focused investigation (including U_3Si_2) by Johnson et al.,¹³ the authors concluded that the oxidation of U_3Si_2 in air and water led to the formation of U_3O_8 and SiO . On further oxidation, SiO may be oxidized to SiO_2 which is relatively more stable compared to SiO .

There exist, however, limited studies aimed at unravelling the interactions of oxygen and water with U_3Si_2 surfaces.¹¹ With the mechanism of the early oxidation of U_3Si_2 surfaces yet to be established, this investigation is timely. Bo et al.¹¹ studied the adsorption and dissociation of H_2O on the (001) surface of uranium mononitride (UN) based on DFT+U calculations and ab initio thermodynamics. They also showed that the UN(001)

^aDepartment of Mechanical Engineering, College of Engineering, University of Saskatchewan, 57 Campus Drive, Saskatoon, S7N 5A9, Saskatchewan, Canada. E-mail: ericmoore.jossou@usask.ca; Fax: +1 (306) 966 5427; Tel: +1 (306) 966 7752

^bDepartment of Earth Sciences, Utrecht University, Princetonplein 9, 3584 CC, Utrecht, The Netherlands

^cDepartment of Physics and Engineering Physics, College of Art and Science, University of Saskatchewan, 116 Science Place, Saskatoon, S7N 5E2, Saskatchewan, Canada

surface reacts readily with water at ambient temperature which leads to oxidation of the UN material. It was suggested that the water molecule dissociates into OH and H species via three pathways with small energy barriers. More recently, Tegner et al.¹² studied the adsorption of H₂O on the {111}, and {110} and {100} surfaces of UO₂ and PuO₂ respectively, using DFT+U. They found a mix of molecular and dissociative water adsorption on the {111} surface, while the full dissociation is dominant on the {110} and {100} surfaces. In this work, we experimentally establish the oxidation of U₃Si₂ in the presence of oxygen and have provided an atomistic insight into the mechanisms of the early oxidation of U₃Si₂ surfaces using Hubbard-corrected density-functional theory (DFT+U) calculations of the reactions of O₂ with the {110}, {001} and {111} surfaces, considering both the molecular and dissociative adsorptions.

2. Experimental setup and computational methodology

2.1. Characterization of U₃Si₂ samples: experimentation

The as-received and oxidized U₃Si₂ sample matrices were characterized by means of spectrochemical and surface microscopy. Raman spectroscopy was deployed in studying the functional chemistry between these samples using a Renishaw Raman InVia reflex microscope (Renishaw, UK). The Raman spectroscopic measurements for the respective samples were performed by varying the acquisition time for an improved signal-to-noise ratio. 100% laser power was attenuated for each trial to avoid sample damage or change of phase; this was conducted at 16 complete scans using a 514 nm laser. A Bruker D8 Discover XRD Diffractometer operating with Cr/K(α) radiation was also used for probing their diffraction patterns. For both samples, the XRD spectra were collected between 10 and 1001 and analyzed using Philips X'Pert software. Surface analysis of these powders was conducted using a scanning electron microscope (Hitachi, SU6600, Japan) at an acceleration voltage of 30 kV.

2.2. Computational details

The first-principles calculations were performed within the plane-wave pseudo-potential DFT technique,^{14,15} as implemented in the Quantum ESPRESSO code.¹⁶ The exchange–correlation functional potential is described by the generalised gradient approximation (GGA) in the Wu–Cohen (GGA-WC) formulation.¹⁷ All our calculations use the norm-conserving Wu–Cohen (WC) pseudopotentials where these potentials treat 7p⁰ 6d¹ 5f³ 7s¹ as valence electrons for U and 3s² 3p⁶ as valence electrons for Si. Due to the on-site Coulomb repulsion among the localized U 5f electrons, we used the Hubbard (DFT+U) approximation to account for the strong electronic correlation effect.¹⁸ We employed an effective value (U_{eff}) of 1.5 eV which was obtained from a recently first-principles study of the U–Si system by Noordhoek et al.¹⁹ showing that the effect of the metastable state in U₃Si₂ is quite small due to the fact that the enthalpy difference for GGA+U calculations with $U_{\text{eff}} = 1.5$ eV for U₃Si₂ with and without the U-ramping method²⁰ is about 0.01 eV atom⁻¹.

Other methods such as quasi-annealing²¹ and occupation matrix control²² have been employed by other investigators to tackle the metastable state difficulty associated with uranium oxides but are beyond the scope of the present study. The Fermi surface effects were treated by the smearing technique of Methfessel–Paxton,²³ using a smearing parameter of 0.02 Ry (0.27 eV). An energy threshold defining the self-consistency of the electron density was set to 10⁻⁸ eV and a beta mixing factor of 0.3. Brillouin zone integration was done using 7 7 10 and 5 5 1 Monkhorst–Pack¹⁶ k-point grids (centred at the G point) for the bulk U₃Si₂ and the surface models, respectively. Structural relaxation was carried out to minimize the energy using the conjugate gradient method within the Broyden–Fletcher–Goldfarb–Shanno (BFGS) algorithm,²⁴ until the magnitude of the residual Hell–Feynman force on each relaxed atom reached 0.01 eV Å⁻¹. Visualization and analysis of the structures were performed using the VESTA program.^{25,26}

The bulk U₃Si₂ was modelled in the tetragonal structure as shown in Fig. 1 in the non-magnetic state as reported by Remischnig et al.²⁷ An earlier DFT (GGA/PBE) calculation performed by Noordhoek et al. predicted a ferromagnetic phase,¹⁹ but here and in our previous study, we realized that using local density approximation (LDA) and generalized gradient approximation (GGA/WC) the predicted binding energies of U₃Si₂ with non-magnetic ordering are 1.13 eV (LDA) and 1.19 eV (GGA/WC) more stable than the ferromagnetic phase in agreement with the experimental observation²⁷ and our earlier calculations using the CASTEP code and the same functional.^{17,28} The different surface structures were created from the fully optimized bulk structure in order to eliminate the presence of fictitious forces during surface relaxation. Surfaces were created using the META-DISE code,²⁹ which not only considers periodicity in the plane direction but also provides the different atomic layer stacking resulting in a zero dipole moment perpendicular to the surface plane, as required for reliable and realistic surface calculations. A vacuum of 15 Å was introduced to the surface models in the z-direction, which is large enough to avoid any spurious inter-actions between periodic slabs. The relative stabilities of the U₃Si₂ surfaces were determined according to their relaxed surface energy (γ_r) in eqn (1):

$$\gamma_r = \frac{1}{4} \frac{E_{\text{slab}}^{\text{relaxed}} - nE_{\text{bulk}}}{2A} \quad (1)$$

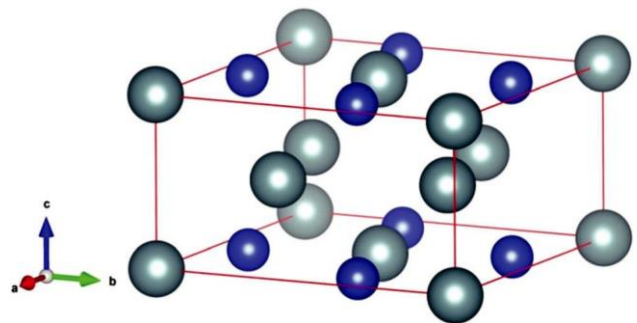


Fig. 1 Schematic illustration of the tetragonal structure of U₃Si₂ (colour scheme: U = grey, Si = blue).

In this equation, $E_{\text{slab}}^{\text{relaxed}}$ is the slab energy with all atomic coordinates relaxed unconstrainedly; nE_{bulk} is the energy of an equal number (n) of bulk U_3Si_2 atoms; A is the area of the slab surface; and the factor of 2 reflects the fact that there are two surfaces for each slab. The unrelaxed surface energy (g_u) was obtained by keeping the atomic coordinates of the slab atoms fixed at the bulk parameters. The calculated unrelaxed and relaxed surface energies of the different low-Miller index U_3Si_2 surfaces are presented in Table 2. We considered several unique geometric orientations for the oxygen molecule adsorption for each surface in this work. The oxygen molecule was modelled in the spin triplet state for all the cases and was introduced onto the surfaces in a vertical (end-on) or horizontal (side-on) orientation. The charge transfer between the O_2 - U_3Si_2 systems was characterized using the Bader topological method.³⁰

3. Results and discussion

3.1. Bulk properties of U_3Si_2

U_3Si_2 is a tetragonal structure with the space group of $P4/\text{mbm}$ (127) and has ten atoms in the conventional unit cell (Fig. 1). The structure is obviously of the Cu_3Au -type with a U atom located at the Cu site and a pair of Si atoms in the position of

Table 1 Optimized structural parameters of U_3Si_2 with $U_{\text{eff}} = 1.5$ eV using GGA/WC pseudopotential

	This work			Literature		
	GGA+U		Expt. ²⁷	GGA+U ^{4,19}		
	GGA	U = 1.5 (4.0) eV		GGA	U = 4.0 eV	U = 1.5 eV
a (Å)	7.17	7.21 (7.48)	7.3151	7.14	7.32	7.479
b (Å)	7.17	7.21 (7.48)	7.3151	7.14	7.32	7.479
c (Å)	3.79	3.86 (3.87)	3.8925	3.89	3.92	3.975
V (Å ³)	194.94	200.66 (216.53)	208.29	198.31	210.04	222.34

the single Au atom. From experimental measurement, the lattice parameters are $a = b = 7.33$ Å, $c = 3.98$ Å, $c/a = 0.543$; $a = b = g = 90$.²⁷ There are two symmetrically distinct U sites occupying the 2a and 4h Wyckoff positions and Si occupies the 4g site. The above reported experimental structural parameters were used as the starting point for our DFT calculations.

Table 1 presents the calculated lattice parameters of U_3Si_2 , with Hubbard-corrected DFT+U values showing close agreement with experiment rather than the standard DFT values. The calculated lattice parameters and unit cell volume compare closely with the previously reported theoretical data.⁴

The electronic structure of U_3Si_2 was determined through analyses of the band structure and the projected density of states (PDOS) as shown in Fig. 2. It is evident from both the band structure and PDOS that U_3Si_2 is metallic with the energy band crossing the Fermi level. It can be seen in the PDOS that the conduction band is composed of a significant hybridization of the uranium 5f states with the silicon 2p states. The U atoms act as the charge carriers and the 5f electrons as conduction electrons as observed in the region around the Fermi energy which is predominantly the uranium f electrons. This is typical of the U-Si compounds as shown in the DFT calculations by Zhang et al.³¹ The nature of bonding is further elucidated qualitatively by the electron density plot in Fig. 2d which shows the formation of a covalent bond between adjacent Si atoms, while the U-Si atoms form an ionic bond evidenced by the lack of a diffuse electron density between the neighbouring U-Si atoms. The result of band structure calculation along the highly symmetric points in the Brillouin zone (Fig. 2e) reveals several dispersive bands mainly from the U 5f across the Fermi level, especially along the R-G direction. The Fermi energy is set at 0 eV as indicated by the horizontal line. There is also an appreciable band overlap between the valence and conduction states, which is responsible for the metallic nature of U_3Si_2 and

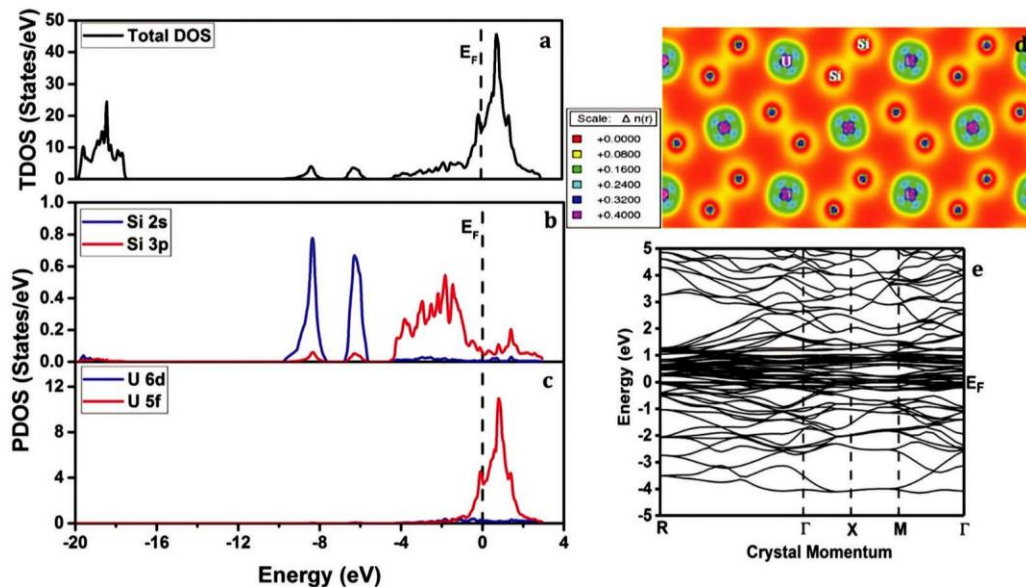


Fig. 2 (a-c) The total and partial density of states (d) electron density map and (e) the band structure of the bulk U_3Si_2 .

the significant amount of electrons at the Fermi level, $N(E_F)$ implies that the high electronic contribution to the heat capacity and the thermal conductivity of U_3Si_2 is mainly due to the U 5f state.

3.2. Evidence of oxidation

3.2.1 Chemistry of samples and morphology. The Raman spectra of the pure and oxidized U_3Si_2 samples depicted in Fig. 3(a) were collected with the aid of 5 and 50 long-focus objectives designed for 785 nm lasers. The distinct peaks related to a possible $\nu(U_{Si})$ stretching vibration within U_3Si_2 can be observed at 1591 cm^{-1} while the uranyl symmetric and antisymmetric stretching bands are represented at 827 and

479 cm^{-1} .³² The Raman band at 445 cm^{-1} broadens, and this may be attributed to increased local disorder. The low intensity $\nu(UO_2)^{2+}$ type band could be linked with the oxidative changes occurring within the bulk of the sample upon storage or exposure to the atmosphere. This must have been due the formation of a thin adsorbed oxide film on the sample. Similar vibration bands are also observed in the Raman spectrum of the oxidative product, and the difference in the peak patterns between the two systems is suggestive of thermal oxidation.

Upon oxidation, new Raman peaks are formed between 800 and 1500 cm^{-1} . The bands around 1150 cm^{-1} are some of the defining Raman peaks characteristic of the oxidative sample. According to Rao et al.,³³ this assignment is attributed to a second-order longitudinal optical (2LO) phonon, being evidence of oxidation. Driscoll et al.³² have also opined that the low intensity Raman bands between 390 and 480 cm^{-1} are related to silicate antisymmetric bending vibrations. To complement the results from Raman spectroscopy, we also conducted XRD studies of these samples. As displayed in Fig. 3(b), the XRD patterns reveal some unique features; data fitting offered a reliable error estimation between both systems owing to their varying chemical environments. There is a trace difference

inherent in the diffraction patterns due to their amorphous solid phases. As expected of pure U_3Si_2 , there are a few diffraction peaks between $2\theta = 10$ and 100° representing the $\{111\}$, $\{200\}$, $\{880\}$, $\{311\}$ and $\{702\}$ planes in line with the ditetragonal dipyramidal body centered crystal structure of U_3Si_2 . Unlike the asymmetric broadening observed for the U_3O_7 tetragonal phase

in ref. 34, there appears to be no such pattern between the $\{200\}$ and $\{002\}$ diffraction lines for U_3Si_2 . The XRD pattern of the oxidized sample reveals more diffraction patterns due to the formation of more oxide phases. According to Rousseau et al.,³⁴ the observed asymmetric diffraction broadening peaks at $\{200\}$ and $\{002\}$ are indicative of a higher oxide; the authors have reported the tetragonal phase associated with U_3O_7 . Upon fitting with Rietveld refinement, Gracia et al.³⁵ have attributed the inability to reconcile some of the X-ray diffracted peaks to the preferential orientation and granulometry, and arrangement of the U_3Si_2 atoms. The surface analysis of the pure U_3Si_2 powders was also conducted using SEM, and Fig. 4 represents the micro-structure and elemental composition of the compound. As observed, Fig. 4(a) is an uneven surface with intermittent grooves enriched with powdered amorphous granules of a secondary USi phase (see the inset). From our experience, the development of this second phase as depicted in Fig. 2(b) is a consequence of the choice preparatory metallurgy technique deployed in synthesis. White et al.³ have observed a similar trend upon synthesizing U_3Si_2 from pure U and Si; the authors also reported significant Si loss due to arc melting-induced volatilization. The formation of new phases of secondary products is also promoted by the inability to control reaction conditions, not limited to temperature, during synthesis. According to White et al.,¹ this unique behaviour could be further explained by monitoring the phase transformations at various temperatures as represented in a typical U–Si partial phase diagram in Okamoto's work.³⁶ For Garcia et al.,³⁵ the product matrix from common synthetic routes comprise two crystalline regular phases (U_3Si_2 and USi) within the same sample with entirely different irradiation behaviors.

3.3. Ab initio surface characterization

Prior to studying the adsorption and surface reaction of oxygen, we have characterized the structure and relative stabilities of the $\{001\}$, $\{110\}$, and $\{111\}$ surfaces which are commonly observed crystallographic planes in tetragonal Cu_3Au -type structures. Fig. 5 presents the optimized structures of the clean surfaces of U_3Si_2 , while Table 2 summarizes the calculated surface energies of the clean surfaces. The surface energies of the clean $\{110\}$, $\{001\}$, and $\{111\}$ surfaces are calculated to be 2.57 , 2.82 , and 2.97 J m^{-2} respectively, which implies that the

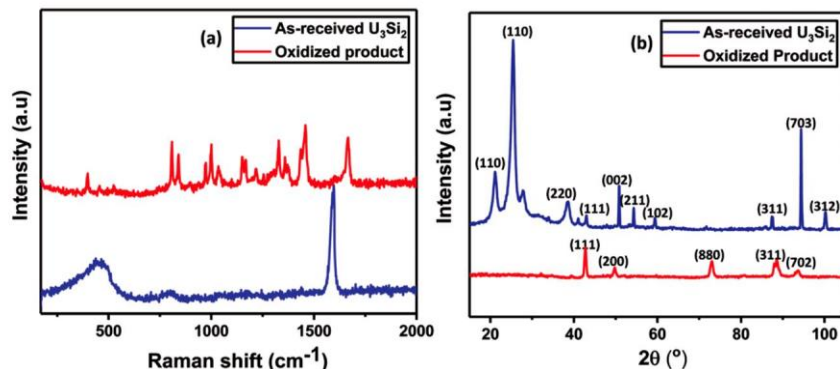


Fig. 3 Representative (a) Raman and (b) XRD spectra of pure U_3Si_2 and its oxidized form.

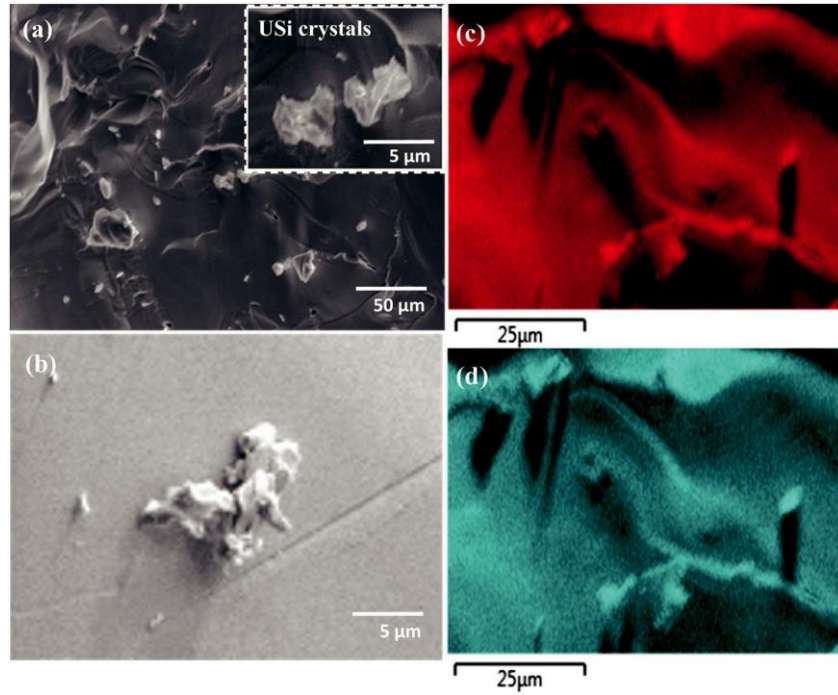


Fig. 4 SEM micrograph showing the pure U_3Si_2 sample (a); the powdered granule develops a secondary USi phase as observed in the amorphous grains displayed in insets (a) and (b); the elemental U Ma1 (80%) and Si Ka1 (15%) maps are presented in (c) and (d), respectively.

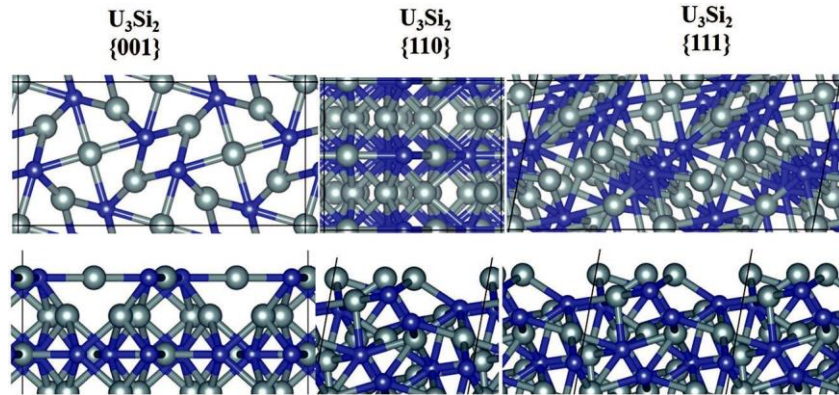


Fig. 5 The optimized structure of the $U_3Si_2\{001\}$, $\{110\}$ and $\{111\}$ surfaces showing the top and bottom views respectively.

Table 2 Calculated surface energies of pristine (g_r) U_3Si_2 low miller index surfaces^a

Surface	g_u (J m ⁻²)	g_r (J m ⁻²)	% Relaxation
{110}	2.58	2.57	0.39
{001}	3.03	2.82	6.77
{111}	3.00	2.97	1.00

^a The corresponding percentage relaxation after surface relaxation is denoted as % relaxation.

order of the decreasing stability of the U_3Si_2 surfaces is $\{110\}$ \circ $\{001\}$ \circ $\{111\}$. Using the calculated surface energies, we constructed the thermodynamic crystal morphology of U_3Si_2 .

The equilibrium morphologies of the U_3Si_2 crystal was constructed according to Wulff's theorem, which states that a

polar plot of surface energy versus the orientation of normal vectors would give the crystal morphology based on the approach of Gibbs.³⁶ The calculated morphology of U_3Si_2 in Fig. 6 shows facets of the clean U_3Si_2 crystal which appears like the frustum of a pyramid with the facet corresponding to the $\{111\}$ orientation forming the top surface and protruding outward with almost a square shape.

As commonly observed at material surfaces, the geometry relaxation of the U_3Si_2 surfaces slightly altered the positions of the surface atoms and therefore their interlayer spacing, which is characterized using the relation:

$$D_{dij} = \frac{1}{4} \frac{d_{ij} d_{bulk}}{d_{bulk}} \times 100;$$

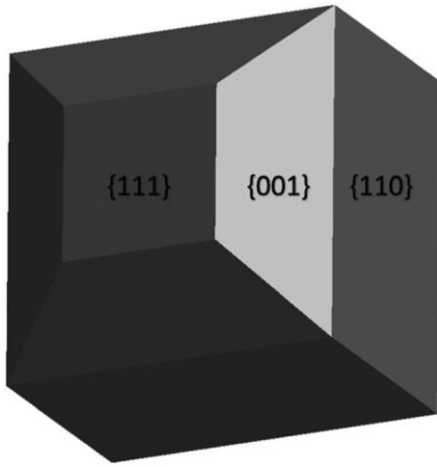


Fig. 6 Wulff construction of the equilibrium crystal morphology of U_3Si_2 .

Table 3 Surface relaxation of the unreconstructed clean surface of U_3Si_2

d _{ij} /surface	Interlayer spacing relaxation (%)		
	{001}	{110}	{111}
d ₁₂	+2.27	24.90	0.12
d ₂₃	+0.93	0.52	0.61
d ₃₄	+0.19	0.08	0.04
d ₄₅	2.25	+22.20	30.52

where the negative values imply inward relaxation (contraction), while the positive values denote outward relaxation (expansion)

of the interlayer spacing. When a crystal is cut to expose a surface, the charge density is redistributed at the surface such that the charge is moved from the regions directly above the atom cores to the regions between the atoms.³⁷ This accounts for the adjustments in the interlayer spacing perpendicular to the surface and there is no change either in the periodicity parallel to the surface or the symmetry of the surface.³⁸ The extent of interlayer relaxation is small on the topmost layer of the {001} and {111} surfaces compared to the {110} surface with a contraction of 24.90 as presented in Table 3.

3.4. Oxygen adsorption

The adsorption of the oxygen molecule on the U_3Si_2 surfaces is an important starting step towards understanding its early oxidation mechanisms. The first point of interest of this study is therefore determining the lowest-energy adsorption structures and modes of oxygen on the low-index U_3Si_2 {001}, {110} and {111} surfaces, and characterizing the strength of their interaction and the extent of the O–O bond elongation. The latter is characterized by charge transfer into the partially filled p_{2p} orbital. Different O₂ initial adsorption possibilities, including side-on and end-on configurations, have been subjected to geometry optimisation until the residual forces on all atoms were $0.03 \text{ eV } \text{\AA}^{-1}$. The adsorption energy (E_{ads}), which is a measure of the strength of the O₂– U_3Si_2 interactions, is defined as follows:

$$E_{\text{ads}} = E_{\text{surface+O}_2} - (E_{\text{surface}} + E_{\text{O}_2}), \quad (2)$$

where $E_{\text{surface+O}_2}$ is the total energy of the substrate–adsorbate system in the equilibrium state, E_{surface} and E_{O_2} are the total energies of the substrate with a clean surface and the free O₂ molecule in the spin triplet state, respectively. By this definition, a negative value of E_{ads} indicates an exothermic and stable adsorption, whereas a positive value indicates unstable adsorption.

3.4.1 Adsorption of molecular and dissociated oxygen on the U_3Si_2 {001} surface. For the adsorption of molecular oxygen on the U_3Si_2 {001}–U–Si terminated surface, we have considered two adsorption modes; the end-on type, where O₂ vertically binds to the surface atom, and a side-on type, where O₂ binds parallel to the surface atom. Fig. 7 presents the optimized adsorption structures of molecular and dissociative O₂ adsorption at various high symmetry sites on the U_3Si_2 {001}–U–Si terminated surface. The calculated adsorption energies, interatomic bond distances and average Bader charge are presented in Table 4. Generally, we found that the U sites are more active toward O₂ adsorption than the Si sites as reflected in the stronger adsorption energies calculated for the U sites. For the adsorption of molecular oxygen on the U_3Si_2 {001} surface, the strongest and the most stable adsorption configuration is calculated for the side-on U–Si bridge (M2) adsorption with an adsorption energy of 3.80 eV, compared to 3.29 eV for the side-on top-U site (M6) adsorption and 3.52 eV for the head-on top-U site (M4) adsorption. In the

lowest-energy molecular O₂ structure (M2), the Si–O and U–O

bond lengths are calculated to be 1.720 and 2.221 Å, respectively,

whereas in the M1 adsorption mode, the Si–O bonds are converged at 1.697 and 1.662 Å, respectively with an adsorption energy of 2.86 eV, suggesting the formation of mixed oxides of uranium and SiO₂ in the M2 configuration since the results are in close agreement with experimental and DFT bond distances of 1.618 Å³⁹ for Si–O and 1.989–2.12 Å^{40–43} for U–O respectively. The formation of intermediate oxides starting with UO₂ which subsequently oxidizes to U₃O₇/U₄O₉ and terminates at U₃O₈ has been proposed recently by two independent studies which is reflected in the range of U–O bond distances calculated in this study.^{6,13} The unusual formation of Si–O bonds here is due to the difference in the electronegativity of Si (1.887) and O (3.758),⁴⁴ and hence O draws charges from Si as shown by the 1.73 e drawn by the O species coupled with the unique arrangement of the {001}–U–Si surface termination.

It is interesting to note that the formation of SiO₂ is desirable on the U_3Si_2 surface as it forms a passivation layer that can prevent further oxidation. This reaction is thermodynamically unfavourable compared to UO₂ formation in the bulk U_3Si_2 experimentally⁶ and we suggest that surface modification or treatment, and the method of synthesis might make a certain crystallographic plane that favours SiO₂ formation to become dominant. Furthermore, the orientation of the oxygen molecule also plays an important role in the formation of the mixed oxides. It is well known that the exposure of certain crystal planes play an important role in determining the surface dependent properties of materials. This understanding has led to the synthesis of high index {311} CuO₂ crystals with enhanced catalytic properties in the oxidation of CO. Also,

crystal and morphology controlled g-Fe₂O₃ has been prepared

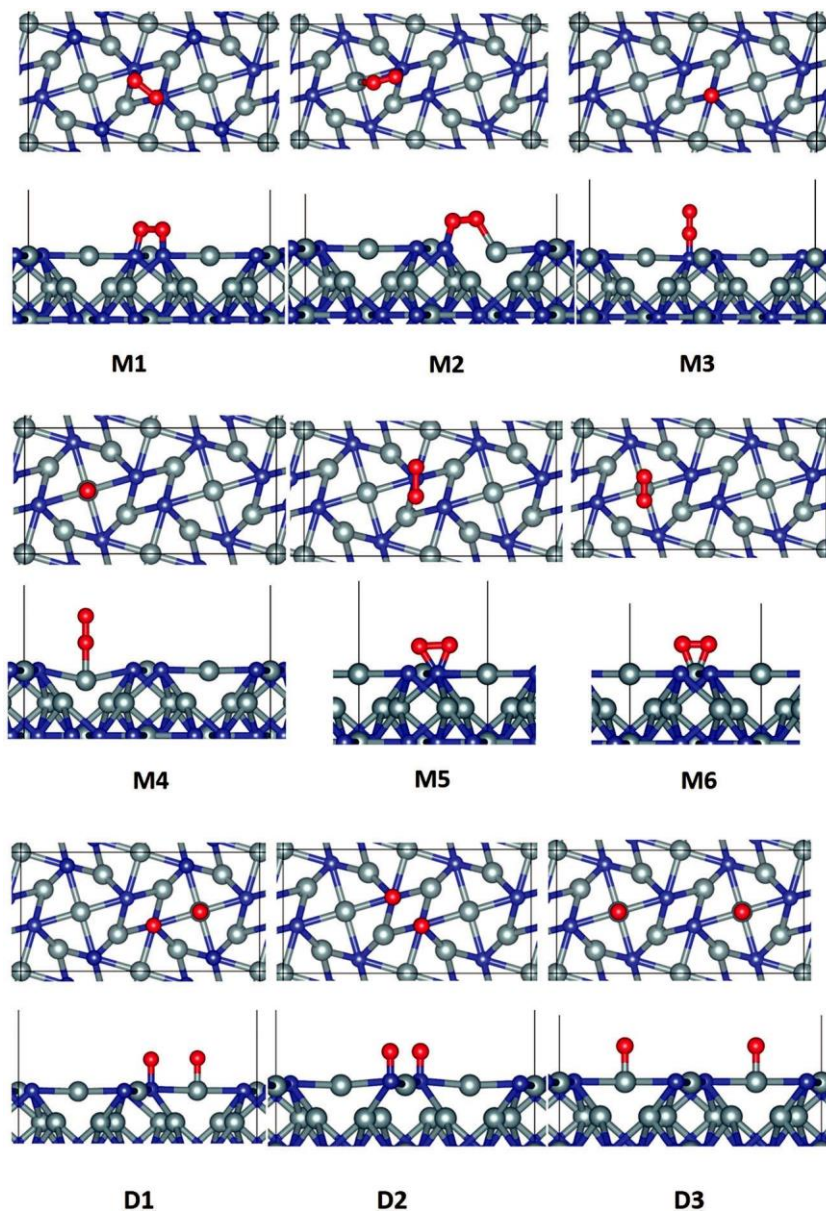


Fig. 7 Top and side views of the relaxed adsorption structures of molecular oxygen adsorbed at Si-bridge sites (M1), U-Si bridge sites (M2), head-on at top Si site (M3), head-on at top U site (M4), side-on at top-Si site (M5), and side-on at top-U site (M6); dissociated oxygen at adjacent top U-Si sites (D1), at adjacent top-Si sites (D2), and at adjacent top-U sites (D3) respectively, on the $\text{U}_3\text{Si}_2\{001\}$ -Si terminated surface. (Color scheme: U = grey, Si = blue, and O = red.)

with reactive $\{110\}$ and $\{100\}$ planes that favours the catalytic reduction of NO with NH_3 .^{45–47}

In the molecular adsorption of oxygen at U sites, the adsorption energies for the side-on (M6) and the head-on (M4) configurations are calculated to be 3.39 eV and 3.52 eV, respectively which implies that the formation of UO_2 is more feasible compared to SiO_2 especially when the M5 configuration is compared where the two Si–O bonds are calculated to be 1.829 and 1.932 Å with an adsorption energy of 1.97 eV. The two U–O bonds in the M6 structure are 2.023 and 2.023 Å, whereas in the M4 structure it is calculated to be 2.213 Å. This thermodynamically showed the preferential formation of UO_2

on the $\{001\}$ surface which has been established in previous work and support the results from the XRD and Raman spectroscopy presented in this work. The least stable molecular O_2 structure is calculated for the case in which the O_2 adsorbed at the Si–Si bridge sites (M3), which released an adsorption energy of 0.50 eV, with the Si–O bond distance converged at 1.590 Å as shown in Table 4. In molecularly adsorbed O_2 at the $\text{U}_3\text{Si}_2\{001\}$ surface, we observed the elongation of the O–O bond lengths (1.392–1.669 Å), which can be attributed to the significant charge gained by the O_2 molecule upon adsorption as shown in Table 4. The elongated O–O bonds in the adsorbed O_2 , especially in the M2 and M6 structures, suggest that these molecular states are likely precursors for O_2 dissociation.

Table 4 Calculated adsorption energy (E_{ads}), relevant bond distance (d), of molecular (O_2) and dissociated ($\text{O}-\text{O}$) oxygen on the $\{001\}$, $\{110\}$ and $\{111\}$ surfaces of U_3Si_2

Surface	Adsorbate	Config.	E_{ads}/eV	$d(\text{O}-\text{O})/\text{\AA}$	$d(\text{Si}-\text{O1})/\text{\AA}$	$d(\text{Si}-\text{O2})/\text{\AA}$	$d(\text{U}-\text{O1})/\text{\AA}$	$d(\text{U}-\text{O2})/\text{\AA}$	Dq/e
{001}-U-Si termination	O_2	M1	2.86	1.639	1.697	1.662	—	—	1.00
		M2	3.80	1.396	1.720	—	2.221	—	2.49
		M3	0.50	1.392	1.590	—	—	—	1.62
		M4	3.52	1.564	—	—	2.213	—	1.48
		M5	1.97	1.669	1.829	1.932	—	—	0.85
		M6	3.29	1.414	—	—	2.023	2.023	2.02
	O-O	D1	4.63	—	1.808	—	1.960	—	1.60
		D2	4.87	—	1.615	1.643	—	—	2.18
		D3	1.37	—	—	—	1.978	1.977	0.74
{001}-U termination	O_2	M1	0.80	1.294	—	—	2.226	—	1.61
		M2	3.64	1.446	—	—	2.243	2.224	2.86
	O-O	D1	4.56	—	—	—	2.126	2.080	1.73
{110}-U-Si termination	O_2	M1	2.26	1.508	2.152	2.105	—	—	1.73
		M2	2.36	1.662	—	—	2.310	2.356	1.50
		M3	0.35	1.290	1.612	—	—	—	1.31
		M4	0.68	1.500	—	—	2.691	—	1.50
	O-O	D1	3.53	—	—	—	—	—	0.68
		D2	3.37	—	1.517	1.542	—	—	0.52
		D3	3.73	—	—	—	2.404	2.313	2.84
{111}-U termination	O_2	M1	2.73	1.548	—	—	2.465	2.805	2.14
	O-O	D1	5.06	—	—	—	2.193	2.238	1.25
		D2	4.11	—	—	—	1.932	1.952	2.10

We have therefore determined the energetics of the dissociative adsorption of oxygen on the $\text{U}_3\text{Si}_2\{001\}$ surface as shown in Fig. 7 (D1–D3). The lowest-energy dissociative O_2 adsorption structure is obtained for the case in which the dissociated O atoms are adsorbed at the adjacent Si sites, with an adsorption energy of 4.87 eV and the average Si–O bond distance at 1.629 Å. A similar adsorption energy (4.63 eV) was calculated for the case in which one of the dissociated O atoms is adsorbed at the Si site (Si–O = 1.808 Å) and the other at the U site (U–O = 1.960 Å). Compared to the lowest-energy molecular adsorption structure (M1), both the dissociative D1 and D2 structures are thermodynamically more stable, suggesting that on the $\text{U}_3\text{Si}_2\{001\}$ surface, oxygen may exist preferentially in a dissociative state at Si sites. When the dissociated O atoms are adsorbed at distant U sites, the least dissociative adsorption energy of 1.37 eV was released. The weaker adsorption of the atomic oxygen species at the U sites compared to the Si sites,

here suggests that the Si sites are active towards dissociated oxygen adsorption. The dissociative adsorption of O_2 at the $\text{U}_3\text{Si}_2\{001\}$ surface is found to be characterized by significant charge transfer from the interacting surface species into the partially filled p2p orbital. This is not surprising because an experimental work by Wood et al. opined the possibility of an SiO_2 phase formation that is either too small to detect by SEM or as an amorphous phase undetectable by XRD.⁶

To ascertain whether the $\{001\}$ surface will favour SiO_2 formation over UO_2 irrespective of the termination, we have further investigated the adsorption properties of O_2 on an alter-native surface model of the $\{001\}$ which exposes only uranium atoms in the topmost layer as shown in Fig. 8. The molecular end-on (M1) and side-on (M2) configurations released adsorption energies of 0.80 and 3.64 eV, respectively, whereas the dissociative adsorption at adjacent U ion sites (D1) released an adsorption energy of 4.56 eV, Table 4. When compared to similar adsorption

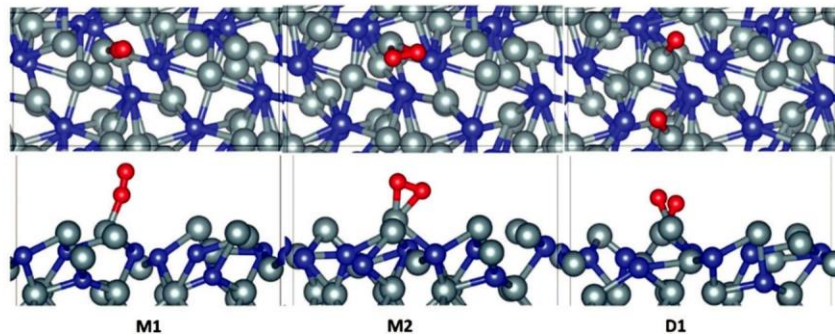


Fig. 8 Top and side views of the relaxed adsorption structures of molecular oxygen adsorbed head-on at top U site (M1), and side-on at top-U site (M2); dissociated oxygen at adjacent top U-U sites (D1), on the $\text{U}_3\text{Si}_2\{001\}$ -U terminated surface. (Colour scheme: U = grey, Si = blue, and O = red.)

configurations on the U–Si terminated {001} surface, we note that the side-on O₂ configuration is 0.35 eV more stable on the U-terminated {001} surface than on the U–Si-terminated surface (Fig. 7 (M6)). The dissociative adsorption mode is also found to be highly stable on the U-terminated surface (4.56 eV) compared to the U–Si-terminated surface (1.37 eV), which suggests that the {001}-U termination is more reactive than the {001}-Si–U-termination. The calculated U–O bond distances (Table 4) compare closely with previous experimental^{40,42} and DFT⁴³ studies and the results suggest the formation of oxides of uranium. When compared to the Si adsorption sites on the {001}-U–Si-terminated surface, we also found that both the calculated molecular side-on O₂ configurations (Fig. 7 (M1 & M5)) are less favored compared to the O₂ side-on adsorption at U sites on both the U–Si and U terminations. The dissociative O₂ adsorption at Si sites on the U–Si termination is however, 0.31 eV more stable than at U sites on the U terminated surface. The thermodynamic favorability of molecular O₂ at the U sites and dissociative O₂ at the Si sites suggests the possibility of a mixed oxide formation (oxides of uranium and SiO₂).

3.4.2 Adsorption of molecular and dissociated oxygen on the U₃Si₂{110} surface. As with the U₃Si₂{001} surface, we have also explored different adsorption sites and binding configurations for O₂ on the U₃Si₂{110} surface in order to determine the lowest-energy adsorption structures. Fig. 9 depicts the lowest-energy

adsorption configuration identified, whereas the calculated adsorption energies, the optimized bond distances and Bader charges for the adsorbed species are reported in Table 4. Compared to the U₃Si₂{001} surface, the molecular oxygen adsorbed side-on at top-U site (M2) on the U₃Si₂{110} surface is observed to bind 0.237 eV more strongly than the side-on adsorption at top-Si site (M1). This is consistent with the preferred formation of the U–O bond compared to the Si–O bond due to the ease of transfer of electrons from a metallic system to the oxygen molecule. It is interesting to note that, when adsorbed at the U-bridge sites (D3), the molecular oxygen spontaneously dissociated into atomic species, with an exothermic adsorption energy of 3.73 eV. The U–O interatomic bond distances are calculated to be 2.404 and 2.313 Å, both of which are close to the U–O bond distance of 2.544 Å observed from the experimental measurements in UO₂.⁴⁸ A total of 2.84 e was transferred from the U to the O molecule. The adsorption energies of the head-on binding mode at top Si site (M3), and the side-on mode at top-U site (M4) are calculated to be 0.352 and 0.677 eV respectively, with a charge transfer of 1.50 e from the U atom and 1.31 e from the Si atom, suggestive of a stronger U–O bond than the Si–O bond as has been observed experimentally.⁶

In this study, the O–O bond becomes generally elongated ranging between 1.290–1.662 Å which on average is similar to a

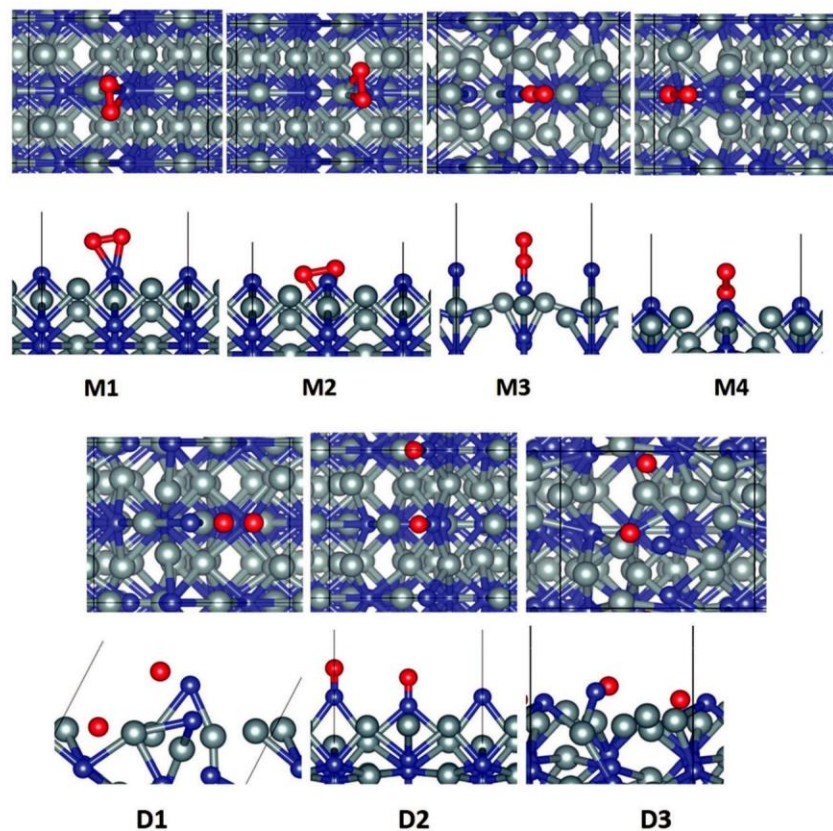


Fig. 9 Top and side views of the relaxed adsorption structures of molecular oxygen adsorbed side-on at top-Si site (M1), side-on at top-U site (M2), head-on at top Si site (M3), and side-on at top-U site (M4); dissociated oxygen at adjacent top U–Si sites (D1), at adjacent top-Si sites (D2), and at U-bridge sites (D3), respectively, on the U₃Si₂{110}-U–Si terminated surface. (Color scheme: U = grey, Si = blue, and O = red.)

peroxo (O_2^2) species with a bond length of 1.40–1.60 Å, suggesting the formation of a peroxo-like (O_2^2) precursor when the molecular oxygen is adsorbed on the $U_3Si_2\{110\}$ surface. The peroxo is often referred to as a precursor for dissociation,⁴⁹ and hence the population of this state of oxygen accounts for the rapid dissociation of molecular oxygen on the $\{110\}$ surface. The significant charge gained by the O_2 molecule upon adsorption, which is characterized by the peroxo (O_2^2) accounts for the elongation of the O–O bond lengths reported here.

The dissociated adsorption of oxygen on the $U_3Si_2\{110\}$ is found to be highly exothermic for the two adsorption sites; at adjacent top U–Si sites (D1), and at adjacent top-Si sites (D2) respectively, with energies of 3.37 and 3.53 eV, respectively. This suggests that oxidation by the dissociated oxygen molecule is generally more stable than molecular oxygen. The preference for dissociative over molecular adsorption is due to the significant charge transfer (0.68 and 0.52 e) from the surface to the O_2 p 2p* orbital weakening the O–O bond, which makes them likely precursors for O_2 dissociation. The same dissociation mechanism has been observed on a number of transition metal surfaces, including Pt(111), Pd(111), Ni(111), Ag(110) and Cu(110)⁵⁰ as well as on actinide metal surfaces such as U–U(100),⁵¹ and Pu(100).⁵²

3.4.3 Adsorption of molecular and dissociated oxygen on the $U_3Si_2\{111\}$ surface. Again, we have explored several possible sites and modes of adsorption of O_2 on the $U_3Si_2\{111\}$ surface as shown in Fig. 10. Table 4 presents the calculated adsorption energies, bond lengths and charge transfers. Molecular adsorption of O_2 at top-U site in a side-on configuration (Fig. 10 (M1)), released an adsorption energy of 2.73 eV. The O–O bond is calculated at 1.548 Å compared to 1.214 Å for the gas phase oxygen molecule, indicating significant elongation upon adsorption. The dissociative adsorption structures Fig. 10 (D1 and D2) of O_2 were calculated to be considerably more stable than the molecular adsorption structure Fig. 10 (M1). When dissociated at adjacent top U-sites (Fig. 10 (D1)), the adsorption energy is calculated to be 4.12 eV, whereas when the dissociated species adsorb at distant U-sites (Fig. 10 (D2)), the adsorption energy is 5.06 eV.

The dissociated O ions, which adsorb preferentially at top-U site (Fig. 3, D1 and D2), draw a combined charge of 1.25 e and 2.10 e respectively from the interacting surface U ions, resulting in their significant oxidation, with the U ions becoming more positively charged compared to the bare U atoms. Similar adsorption

features have been observed in the AnO_2 ($An = U, Pu$ and Am) type oxides where the An –O bonds are preferentially formed compared to An –OH when H_2O dissociates on the surfaces.⁹

3.5. Electronic structures

Insight into the extent of oxidation on the U_3Si_2 surfaces was further explored by calculating and analyzing the density of states (DOS) projected on the oxygen, silicon and uranium atoms in the first layer of the U_3Si_2 surfaces. The density of states (DOS) of a structure indicates the number of states at each energy level which is available to be occupied and the DOS at the Fermi energy level (E_F) quantitatively gives the amount of electrons $N(E_F)$ available for bond formation in a reaction.⁵³ The PDOS of the clean $U_3Si_2\{001\}$, $\{110\}$ and $\{111\}$ surfaces (before O_2 adsorption), with projection on the U f-states and Si p-states are shown in Fig. 11. The U f-states significantly contribute to the DOS around the Fermi level of the three low-index surfaces studied, with only a small contribution from the Si p-states at the Fermi level. The contribution of the U f-states at the Fermi level increases in the order $\{110\} < \{001\} < \{111\}$, which explains why more electrons were transferred from the $\{111\}$ surface to the oxygen molecule compared to the $\{001\}$ and $\{110\}$ surfaces.

For the oxygen-covered surfaces, we have investigated the nature of their interactions with the oxygen molecule by analyzing the PDOS of the interacting U f-states and Si p-states as shown in Fig. 12. We observed hybridization between the U 5f and O 2p states, which is an indication of electron transfer from the interacting U ions to the adsorbed oxygen. This chemical change is confirmed by the electron transfer from the U species to the O ions as evident for the calculated Bader charges.

3.6. Summary and conclusions

We have performed experimental and Density Functional Theory (DFT) investigations of the early oxidation of U_3Si_2 in the presence of adsorbed oxygen molecules. The chemical structure presented by DFT calculation reveals that the oxygen molecule interacts strongly with the U_3Si_2 surfaces, with the adsorption characterized by significant charge transfer from the interacting surfaces to the adsorbing oxygen molecule. The population of the partially filled p2p orbital resulted in the formation of a

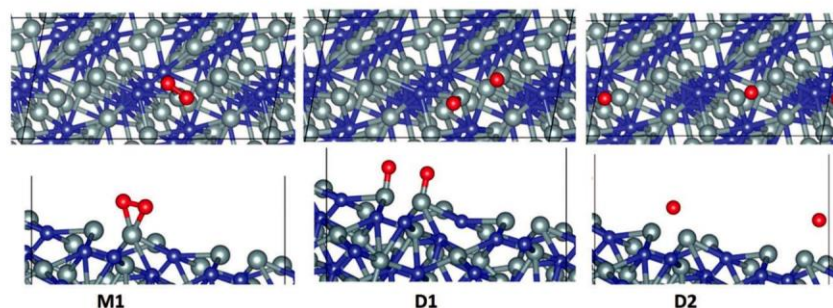


Fig. 10 Top and side views of the relaxed adsorption structures of molecular oxygen adsorbed side-on at top-U site (M1) dissociated oxygen at adjacent top U–Si sites (D1), side-on at top-Si site (D2); on the $U_3Si_2\{111\}$ -terminated surface. (Color scheme: U = grey, Si = blue, and O = red.)

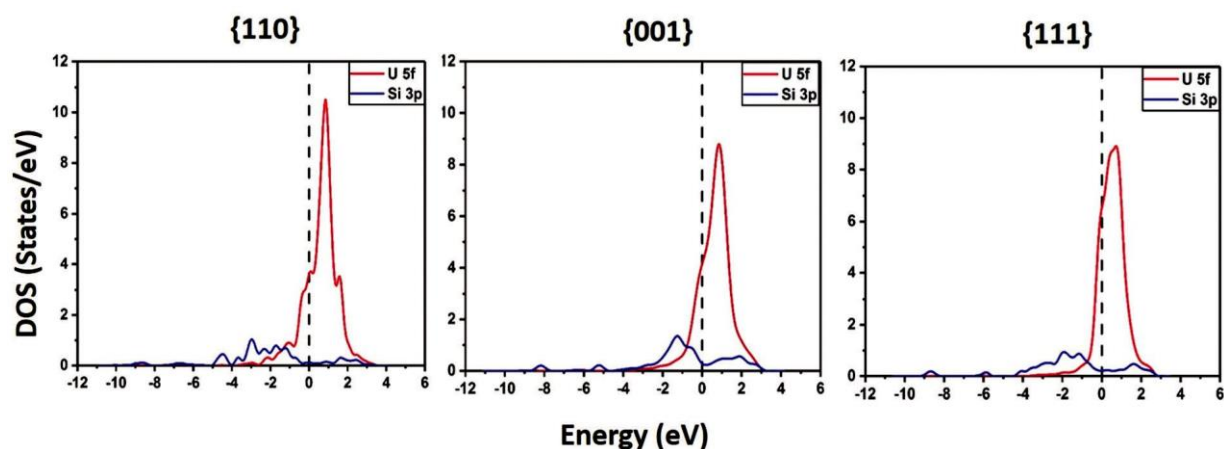


Fig. 11 Electron densities of states of the $\text{U}_3\text{Si}_2\{110\}$, $\text{U}_3\text{Si}_2\{001\}$ and $\text{U}_3\text{Si}_2\{111\}$ naked surfaces projected on the U-f and Si-p states. Electron densities of the U-f states at the Fermi level for the different surface increases in the order $\{110\} < \{001\} < \{111\}$.

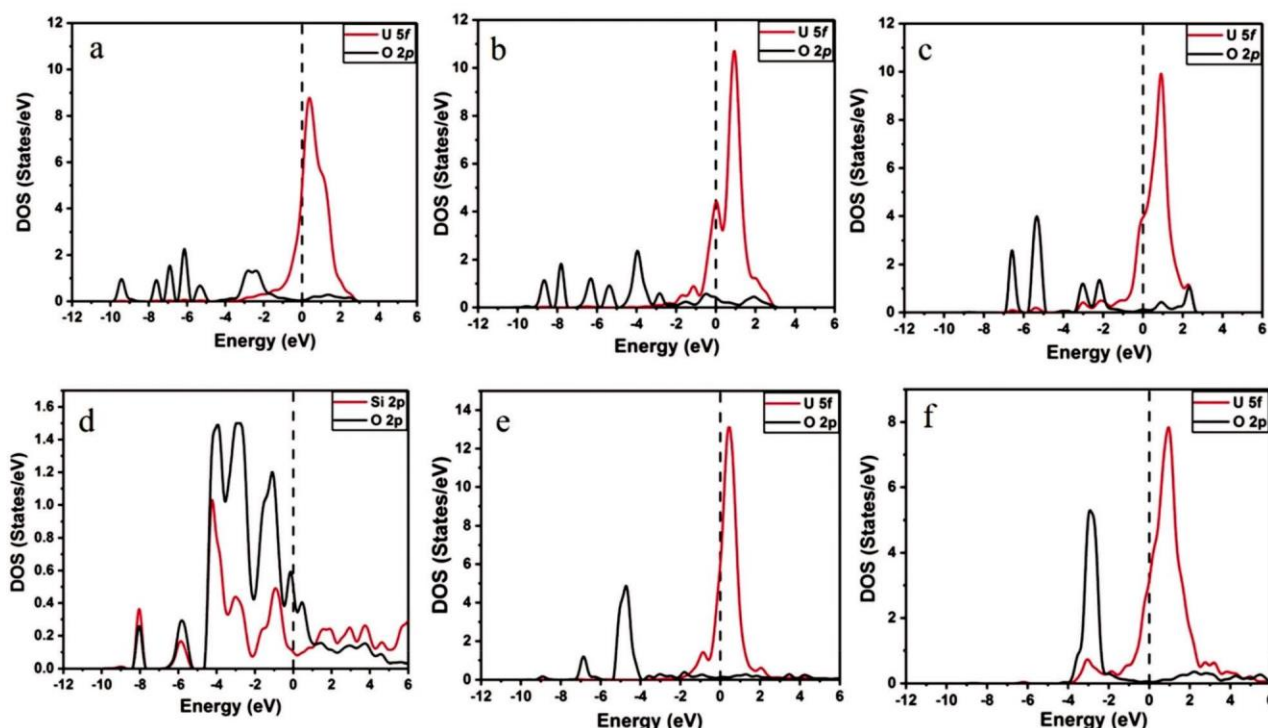


Fig. 12 Partial DOS projected on the interacting surface U f-states and O p-states for adsorbed molecular oxygen for (a) $\{001\}$ (b) $\{110\}$ and (c) $\{111\}$ and adsorbed atomic oxygen for (d) $\{001\}$ (e) $\{110\}$ and (f) $\{111\}$ surfaces respectively.

peroxo-like (O_2^{2-}) species with elongated O–O bonds on the U_3Si_2 surfaces. Generally, the U_3Si_2 surfaces are shown to be easily oxidized by dissociated oxygen molecules which imply that dissociation is a necessary step before the oxidation of U_3Si_2 and this is consistent with the more stable exothermic energies calculated for dissociative compared to molecular adsorption. Core experimental analyses of the oxidized U_3Si_2 samples have revealed the formation of higher oxides from Raman spectroscopy and XRD techniques. The low intensity $\nu(\text{UO}_2)^{2+}$ type bands observed for the pure sample could be linked with the partial oxidative changes on the powder due to the exposure to synthetic air. Its morphology reveals an uneven

surface with intermittent grooves enriched with amorphous granules of a secondary USi phase.

Conflicts of interest

There are no conflicts to declare.

Acknowledgements

The authors gratefully acknowledge Compute Canada (West-Grid) and the University of Saskatchewan's Research Cluster

(Plato) for the generous amount of CPU time. We also acknowledge the financial support from the Canadian National Science and Engineering Research Council (NSERC) and the University of Saskatchewan's International Dean's Scholarship; the Saskatchewan Structural Sciences Centre (SSSC) is also acknowledged for providing some of the facilities for this research. We are grateful to Dr Andrew Nelson from the Los Alamos National Laboratory for providing the U_3Si_2 sample used in this work. Thanks to Ahmed Tamiyu for helping out with the SEM and XRD measurements.

References

- 1 J. T. White, A. T. Nelson, D. D. Byler, D. J. Safarik, J. T. Dunwoody and K. J. McClellan, *J. Nucl. Mater.*, 2015, 456, 442–448.
- 2 J. T. White, A. T. Nelson, D. D. Byler, J. A. Valdez and K. J. McClellan, *J. Nucl. Mater.*, 2014, 452, 304–310.
- 3 J. T. White, A. T. Nelson, J. T. Dunwoody, D. D. Byler, D. J. Safarik and K. J. McClellan, *J. Nucl. Mater.*, 2015, 464, 275–280.
- 4 T. Wang, N. Qiu, X. Wen, Y. Tian, J. He, K. Luo, X. Zha, Y. Zhou, Q. Huang, J. Lang and S. Du, *J. Nucl. Mater.*, 2016, 469, 194–199.
- 5 Y. S. Kim, G. L. Hofman, J. Rest and A. B. Robinson, *J. Nucl. Mater.*, 2009, 389, 443–449.
- 6 E. S. Wood, J. T. White and A. T. Nelson, *J. Nucl. Mater.*, 2017, 484, 245–257.
- 7 L. H. Ortega, B. J. Blamer, J. A. Evans and S. M. McDeavitt, *J. Nucl. Mater.*, 2016, 471, 116–121.
- 8 J. P. W. Wellington, A. Kerridge, J. Austin and N. Kaltsoyannis, *J. Nucl. Mater.*, 2016, 482, 124–134.
- 9 T. Bo, J.-H. Lan, Y.-L. Zhao, Y.-J. Zhang, C.-H. He, Z.-F. Chai and W.-Q. Shi, *J. Nucl. Mater.*, 2014, 454, 446–454.
- 10 G. Jomard, F. Bottin and G. Geneste, *J. Nucl. Mater.*, 2014, 451, 28–34.
- 11 T. Bo, J.-H. Lan, Y.-L. Zhao, Y.-J. Zhang, Y.-L. Zhao, C.-H. He, Z.-F. Chai and W.-Q. Shi, *Phys. Chem. Chem. Phys.*, 2016, 18, 13255–13266.
- 12 B. E. Tegner, M. Molinari, A. Kerridge, S. C. Parker and N. Kaltsoyannis, *J. Phys. Chem. C*, 2017, 121, 1675–1682.
- 13 K. Johnson, V. Stroh, J. Wallenius and D. A. Lopes, *J. Nucl. Sci. Technol.*, 2017, 54, 280–286.
- 14 P. Hohenberg and W. Kohn, *Phys. Rev.*, 1964, 136, B864–B871.
- 15 W. Kohn and L. J. Sham, *Phys. Rev.*, 1965, 140, A1133–A1138.
- 16 P. Giannozzi, S. Baroni, N. Bonini, M. Calandra, R. Car, C. Cavazzoni, D. Ceresoli, G. L. Chiarotti, M. Cococcioni, I. Dabo, A. Dal Corso, S. de Gironcoli, S. Fabris, G. Fratesi, R. Gebauer, U. Gerstmann, C. Gougoussis, A. Kokalj, M. Lazzeri, L. Martin-Samos, N. Marzari, F. Mauri, R. Mazzarello, S. Paolini, A. Pasquarello, L. Paulatto, C. Sbraccia, S. Scandolo, G. Sclauzero, A. P. Seitsonen, A. Smogunov, P. Umari and R. M. Wentzcovitch, *J. Phys.: Condens. Matter*, 2009, 21, 395502.
- 17 Z. Wu and R. E. Cohen, *Phys. Rev. B: Condens. Matter Mater. Phys.*, 2006, 73, 235116.
- 18 A. I. Liechtenstein, V. I. Anisimov and J. Zaanen, *Phys. Rev. B: Condens. Matter Mater. Phys.*, 1995, 52, R5467–R5470.
- 19 M. J. Noordhoek, T. M. Besmann, D. Andersson, S. C. Middleburgh and A. Chernatynskiy, *J. Nucl. Mater.*, 2016, 479, 216–223.
- 20 B. Meredig, A. Thompson, H. A. Hansen, C. Wolverton and A. Van De Walle, *Phys. Rev. B: Condens. Matter Mater. Phys.*, 2010, 82, 2–6.
- 21 H. Y. Geng, Y. Chen, Y. Kaneta, M. Kinoshita and Q. Wu, *Phys. Rev. B: Condens. Matter Mater. Phys.*, 2010, 82, 94106.
- 22 B. Dorado, B. Amadon, M. Freyss and M. Bertolus, *Phys. Rev. B: Condens. Matter Mater. Phys.*, 2009, 79, 235125.
- 23 M. Methfessel and A. T. Paxton, *Phys. Rev. B: Condens. Matter Mater. Phys.*, 1989, 40, 3616–3621.
- 24 J. D. Head and M. C. Zerner, *Chem. Phys. Lett.*, 1985, 122, 264–270.
- 25 K. Momma and F. Izumi, *J. Appl. Crystallogr.*, 2008, 41, 653–658.
- 26 K. Momma and F. Izumi, *J. Appl. Crystallogr.*, 2011, 44, 1272–1276.
- 27 K. Remschnig, T. Le Bihan, H. Noe'l and P. Rogl, *J. Solid State Chem.*, 1992, 97, 391–399.
- 28 B. Szpunar, L. Malakkal, E. Jossou and J. Szpunar, *First Principles Investigation of Alternative Nuclear Fuels: a chapter*, in *Energy Materials*, ed. X. Liu, et al., Springer Press, 2017, pp. 367–376.
- 29 G. W. Watson, E. T. Kelsey, N. H. de Leeuw, D. J. Harris and S. C. Parker, *J. Chem. Soc., Faraday Trans.*, 1996, 92, 433–438.
- 30 R. F. W. Bader, *Acc. Chem. Res.*, 1985, 18, 9–15.
- 31 Y. Zhang and A. D. R. Andersson, *A thermal conductivity model for U–Si compounds*, 2017.
- 32 R. J. P. Driscoll, D. Wolverton, J. M. Mitchels, J. M. Skelton, S. C. Parker, M. Molinari, I. Khan, D. Geesonb and G. C. Allen, *RSC Adv.*, 2014, 4, 59137–59149.
- 33 R. Rao, R. K. Bhagat, N. P. Salke and A. Kumar, *Appl. Spectrosc.*, 2014, 68, 44–48.
- 34 G. Rousseau, L. Desgranges, F. Charlot, N. Millot, J. C. Nie'pce, M. Pijolat, F. Valdivieso, G. Baldinozzi and J. F. Be'rar, *J. Nucl. Mater.*, 2006, 355, 10–20.
- 35 R. H. L. Garcia, A. M. Saliba-Silva, E. F. U. Carvalho, N. B. Lima, R. U. Ichikawa and L. G. Martinez, *INAC, 2013: International Nuclear Atlantic Conference*, Brazil.
- 36 ASM International, *Alloy Phase Diagrams*, ASM Handbook, 1998.
- 37 R. Smoluchowski, *Phys. Rev.*, 1941, 60, 661–674.
- 38 U. Landman, R. N. Hill and M. Mostoller, *Phys. Rev. B: Condens. Matter Mater. Phys.*, 1980, 21, 448–457.
- 39 M. T. Dove, D. A. Keen, A. C. Hannon and I. P. Swainson, *Phys. Chem. Miner.*, 1997, 24, 311–317.
- 40 F. Garrido, A. C. Hannon, R. M. Ibberson, L. Nowicki and B. T. M. Willis, *Inorg. Chem.*, 2006, 45, 8408–8413.
- 41 G. C. Allen, P. A. Tempest. and J. W. Tyler, *Nature*, 1982, 295, 48–49.
- 42 S. D. Conradson, B. D. Begg, D. L. Clarka, C. den Auwer, M. Dinga, P. K. Dorhout, F. J. Espinosa-Faller, P. L. Gordon, R. G. Haire, N. J. Hess, R. F. Hess, D. W. Keogh, G. H. Lander, D. Manarah, L. A. Morales, M. P. Neu, P. Paviet-Hartmann, J. Rebizant, V. V. Rondinella, W. Runde, C. D. Tait, D. K. Veirs,

- P. M. Vilella and F. Wastinh, *J. Solid State Chem.*, 2005, 178, 521–535.
- 43 F. N. Skomurski, J. W. Wang, R. C. Ewing and U. Becker, *J. Nucl. Mater.*, 2013, 434, 422–433.
- 44 K. Li and D. Xue, *J. Phys. Chem. A*, 2006, 110, 11332–11337.
- 45 M. Leng, M. Liu, Y. Zhang, Z. Wang, C. Yu, X. Yang, H. Zhang and C. Wang, *J. Am. Chem. Soc.*, 2010, 132, 17084–17087.
- 46 D. Su, S. Dou and G. Wang, *Sci. Rep.*, 2014, 4, 5767.
- 47 X. Mou, B. Zhang, Y. Li, L. Yao, X. Wei, D. S. Su and W. Shen, *Angew. Chem., Int. Ed.*, 2012, 51, 2989–2993.
- 48 M. Magnuson, S. M. Butorin, L. Werme, J. Nordgren, K. Ivanov, J.-H. Guo and D. K. Shuh, *Appl. Surf. Sci.*, 2006, 252, 5615–5618.
- 49 D. Yu, G. S. Hwang, T. A. Kirichenko and S. K. Banerjee, *Phys. Rev. B: Condens. Matter Mater. Phys.*, 2005, 72, 205204.
- 50 M. Yan, Z.-Q. Huang, Y. Zhang and C.-R. Chang, *Phys. Chem. Chem. Phys.*, 2017, 19, 2364–2371.
- 51 M. N. Huda and A. K. Ray, *Int. J. Quantum Chem.*, 2005, 102, 98–105.
- 52 M. N. Huda and A. K. Ray, *Eur. Phys. J. B*, 2005, 43, 131–141.
- 53 D.-K. Ko and C. B. Murray, *ACS Nano*, 2011, 5, 4810–4817.